Precision Engineering 46 (2016) 65–72

Contents lists available at ScienceDirect

Precision Engineering

journal homepage: www.elsevier.com/locate/precision

A coupled dynamics, multiple degree of freedom process damping model, Part 1: Turning

Christopher T. Tyler, John R. Troutman, Tony L. Schmitz*

University of North Carolina at Charlotte, Charlotte, NC, United States

ARTICLE INFO

Article history:
Received 1 May 2015
Received in revised form 10 February 2016
Accepted 21 March 2016
Available online 12 May 2016

Keywords:
Machining
Chatter
Stability
Process damping
Simulation

ABSTRACT

Self-excited vibration, or chatter, is an important consideration in machining operations due to its direct influence on part quality, tool life, and machining cost. At low machining speeds, a phenomenon referred to as process damping enables stable cutting at higher depths of cut than predicted with traditional analytical models. This paper describes an analytical stability model which includes a process damping force that is dependent on the surface normal velocity, chip width, cutting speed, and an empirical process damping coefficient. Model validation is completed using time domain simulation and turning experiments. The results indicate that the multiple degree of freedom model is able to predict the stability boundary using a single process damping coefficient.

1. Introduction

Process damping is a phenomenon that enables increased depths at cut at low cutting speeds in machining operations. When its effect is added to the analytical stability lobe diagram, a valuable predictive capability is afforded to process planners for a priori selection of machining parameters. It enables process planners to select stable {spindle speed, depth of cut} combinations for both:

- hard-to-machine materials, that are restricted to low cutting speeds due to prohibitive tool wear, and, therefore, cannot capitalize on the increased depths of cut observed in traditional stability lobe diagrams at higher spindle speeds; and
- high machinability materials that are able to take advantage of the increased depths of cut at the "best spindle speeds", which occur at rotating frequencies which are substantial integer fractions of the natural frequency that corresponds to the most flexible structural mode of vibration.

Nearly 50 years of experimental and theoretical investigations have yielded a phenomenological understanding of process damping. Pioneering work was completed by Wallace and Andrew [1], Sisson and Kegg [2], Peters et al. [3], and Tlusty [4]. These studies identified process damping as energy dissipation due to interference between the cutting tool relief, or clearance, face and the machined surface during the inherent relative vibration between the tool and workpiece. It was hypothesized that process damping increases at low cutting speeds because the number of undulations on the machined surface between revolutions (turning) or teeth (milling) increases, which also increases the slope of the wavy surface. This leads to increased interference and, consequently, increased energy dissipation.

Follow-on work has included a plowing force model based on interference between the tool's relief face and workpiece surface [5], application of the plowing force model to milling [6–9], a mechanistic description of the shearing and plowing force contributions to process damping [10], and a first-order Fourier transform representation of the tool-workpiece interference [11,12]. In [13,14], a numerical simulation of a nonlinear process damping stability model was presented, while [15] provided an experimental investigation of a nonlinear process damping model. Experimental identifications of a process damping model were presented in [16,17]. This study builds on the analyses presented in [18–20].

In this paper, an analytical stability analysis is presented that enables multiple degree of freedom (DOF) structural dynamics to be considered, while describing the process damping force in the surface normal direction as a function of the depth of cut, the cutting speed, the tool velocity, and a single empirical coefficient. Because the process damping force is based on the surface normal velocity, which, in general, includes contributions from both orthogonal dynamics directions, a coupled dynamic system is obtained. The analytical solution for turning is presented in the following

* Corresponding author. Tel.: +1 17046875086.
E-mail address: tony.schmitz@uncc.edu (T.L. Schmitz).

http://dx.doi.org/10.1016/j.precisioneng.2016.03.017
0141-6359/

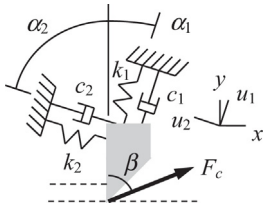

Fig. 1. Turning model with a single DOF in two orthogonal directions.

sections. Validation of the algorithm using time domain simulation and experiments is provided.

2. Stability algorithm

2.1. Single DOF in two directions

The turning model with a single DOF in two orthogonal directions is depicted in Fig. 1. The two mode directions, u_1 and u_2, are oriented at the angles α_1 and α_2, respectively, relative to the surface normal direction, y. The cutting force, F_c, is oriented at the force angle β. The variable component of the cutting force is described by Eq. (1), where K_s is the specific cutting force coefficient, b is the commanded chip width, Y_0 is the vibration amplitude in the y direction from the previous revolution, and Y is the current vibration amplitude. The difference between Y_0 and Y identifies the variable chip thickness due to the vibration from one revolution to the next and provides the basis for regenerative chatter. The mean component of the cutting force is excluded because it does not influence stability for the linear analysis presented here.

$$F_c = K_s b(Y_0 - Y) \tag{1}$$

The assumption for Eq. (1) is that there is no phase shift between the variable force and the chip thickness. This is indicated by the real values of b and K_s. However, it has been shown that a phase shift can occur at low cutting speeds. This phenomenon is captured by the inclusion of the process damping force, F_d, defined in Eq. (2) [17], where C is the process damping coefficient, V is the cutting speed, and $\dot{y}$ is the tool velocity in the y direction. The process damping force is oriented in the y direction and opposes the cutting force (as projected in the y direction). In other words, it is a viscous damping force. Therefore, the process damping force is used to modify the structural damping and obtain an analytical stability solution.

$$F_d = -C\frac{b}{V}\dot{y} \tag{2}$$

To proceed with the solution, the cutting and process damping forces are projected into the u_1 and u_2 directions as shown in Eqs. (3) and (4), where F_{c_1} and F_{c_2} are the cutting force components in the u_1 and u_2 directions.

$$F_{u_1} = F_c\cos(\beta-\alpha_1) - C\frac{b}{V}\dot{y}\cos(\alpha_1) = F_{c_1} - C\frac{b}{V}\dot{y}\cos(\alpha_1) \tag{3}$$

$$F_{u_2} = F_c\cos(\beta+\alpha_2) - C\frac{b}{V}\dot{y}\cos(\alpha_2) = F_{c_2} - C\frac{b}{V}\dot{y}\cos(\alpha_2) \tag{4}$$

The time domain equations of motion for the two directions are provided in Eqs. (5) and (6), where m_i, c_i, and k_i, $i = 1, 2$, are the mass, viscous damping coefficient, and stiffness for the single DOF structural dynamics. In these equations, one overdot indicates one time derivative (velocity) and two overdots indicate two time derivatives (acceleration).

$$m_1\ddot{u}_1 + c_1\dot{u}_1 + k_1u_1 = F_{c_1} - C\frac{b}{V}\dot{y}\cos(\alpha_1) \tag{5}$$

$$m_2\ddot{u}_2 + c_2\dot{u}_2 + k_2u_2 = F_{c_2} - C\frac{b}{V}\dot{y}\cos(\alpha_2) \tag{6}$$

The y direction velocity can be written as a function of the velocities in the u_1 and u_2 directions as shown in Eq. (7). Substitution of Eq. (7) into Eqs. (5) and (6) yields Eqs. (8) and (9). Even though the structural dynamics are uncoupled (orthogonal), the equations of motion for the two directions are now coupled through the $\dot{u}_1$ and $\dot{u}_2$ velocity terms.

$$\dot{y} = \dot{u}_1\cos(\alpha_1) + \dot{u}_2\cos(\alpha_2) \tag{7}$$

$$m_1\ddot{u}_1 + c_1\dot{u}_1 + k_1u_1 = F_{c_1} - C\frac{b}{V}(\dot{u}_1\cos(\alpha_1) + \dot{u}_2\cos(\alpha_2))\cos(\alpha_1) \tag{8}$$

$$m_2\ddot{u}_2 + c_2\dot{u}_2 + k_2u_2 = F_{c_2} - C\frac{b}{V}(\dot{u}_1\cos(\alpha_1) + \dot{u}_2\cos(\alpha_2))\cos(\alpha_2) \tag{9}$$

By assuming a solution of the form $u_1(t) = U_1e^{i\omega t}$ for harmonic motion, Eqs. (8) and (9) can be rewritten in the frequency domain (ω is frequency). The results are provided in Eqs. (10) and (11), where the U_1 and U_2 terms have been grouped on the left hand side in both equations and the $e^{i\omega t}$ term has been dropped from both sides in each case.

$$\left(-m_1\omega^2 + i\omega\left(c_1 + C\frac{b}{V}(\cos(\alpha_1))^2\right) + k_1\right)U_1 + i\omega\left(C\frac{b}{V}\cos(\alpha_1)\cos(\alpha_2)\right)U_2 = F_{c_1} \tag{10}$$

$$\left(-m_2\omega^2 + i\omega\left(c_2 + C\frac{b}{V}(\cos(\alpha_2))^2\right) + k_2\right)U_2 + i\omega\left(C\frac{b}{V}\cos(\alpha_1)\cos(\alpha_2)\right)U_1 = F_{c_2} \tag{11}$$

These equations are arranged in matrix form as shown in Eq. (12), where:

- $a_{11} = \left(-m_1\omega^2 + i\omega\left(c_1 + C\frac{b}{V}(\cos(\alpha_1))^2\right) + k_1\right)$
- $a_{12} = i\omega\left(C\frac{b}{V}\cos(\alpha_1)\cos(\alpha_2)\right)$
- $a_{21} = a_{12}$
- $a_{22} = \left(-m_2\omega^2 + i\omega\left(c_2 + C\frac{b}{V}(\cos(\alpha_2))^2\right) + k_2\right)$.

$$\begin{bmatrix} a_{11} & a_{12} \\ a_{21} & a_{22} \end{bmatrix}\begin{bmatrix} U_1 \\ U_2 \end{bmatrix} = \begin{bmatrix} F_{c_1} \\ F_{c_2} \end{bmatrix} \tag{12}$$

Using complex matrix inversion on a frequency-by-frequency basis, the direct and cross frequency response functions (FRFs) for the coupled dynamic system are obtained as shown in Eq. (13). The direct FRFs are located in the on-diagonal positions and the cross FRFs are located in the off-diagonal positions; the cross FRFs are equal because the inverted matrix is symmetric.

$$\begin{bmatrix} U_1 \\ U_2 \end{bmatrix} = \begin{bmatrix} a_{11} & a_{12} \\ a_{21} & a_{22} \end{bmatrix}^{-1}\begin{bmatrix} F_{c_1} \\ F_{c_2} \end{bmatrix} = \begin{bmatrix} \frac{U_1}{F_{c_1}} & \frac{U_1}{F_{c_2}} \\ \frac{U_2}{F_{c_1}} & \frac{U_2}{F_{c_2}} \end{bmatrix}\begin{bmatrix} F_{c_1} \\ F_{c_2} \end{bmatrix} \tag{13}$$

Tlusty [21] provided a frequency domain stability solution for regenerative chatter in turning, which defines the limiting stable chip width, b_{lim}, using Eq. (14), where $Re(G_{or})$ is the negative portion of the real part of the oriented FRF, G_{or}. This oriented FRF represents the projection of the cutting force into the mode direction and then the projection of this result in the surface normal direction.

$$b_{\text{lim}} = \frac{-1}{2K_sRe(G_{or})} \tag{14}$$

To relate the frequency-dependent b_{lim} vector to the spindle speed, Ω, Eq. (15) is applied to determine the relationship between and the valid chatter frequencies, f_c (i.e., those frequencies where $Re(G_{or})$ is negative). In this equation, $N = 0, 1, 2, \ldots$ is the integer number of waves per revolution (i.e., the lobe number) and

$\varepsilon = 2\pi - 2\tan^{-1}\left(\frac{Re(G_{or})}{Im(G_{or})}\right)$ is the phase between the current vibration and the previous revolution.

$$\frac{f_c}{\Omega} = N + \frac{\varepsilon}{2\pi} \tag{15}$$

Tlusty's approach is extended here to develop an oriented FRF that incorporates both the direct and cross FRFs from Eq. (13). The oriented FRF is defined using Eq. (16), where μ_{ij}, $i, j = 1, 2$, are the directional orientation factors:

- $\mu_{11} = \cos(\beta - \alpha_1)\cos(\alpha_1)$ projects F into u_1 to cause u_1 vibration through the direct FRF U_1/F_{c_1} and then projects this result into y
- $\mu_{12} = \cos(\beta + \alpha_2)\cos(\alpha_1)$ projects F into u_2 to cause u_1 vibration through the cross FRF U_1/F_{c_2} and then projects this result into y
- $\mu_{21} = \cos(\beta - \alpha_1)\cos(\alpha_2)$ projects F into u_1 to cause u_2 vibration through the cross FRF U_2/F_{c_1} and then projects this result into y
- $\mu_{22} = \cos(\beta + \alpha_2)\cos(\alpha_2)$ projects F into u_2 to cause u_2 vibration through the direct FRF U_2/F_{c_2} and then projects this result into y.

$$G_{or} = \mu_{11}\frac{U_1}{F_{c_1}} + \mu_{12}\frac{U_1}{F_{c_2}} + \mu_{21}\frac{U_2}{F_{c_1}} + \mu_{22}\frac{U_2}{F_{c_2}} \tag{16}$$

The direct and cross FRFs included in Eq. (16) incorporate the process damping contribution by modifying the structural damping through the terms: $i\omega(c_1 + C(b/V)(\cos(\alpha_1))^2)$, $i\omega(C(b/V)\cos(\alpha_1)\cos(\alpha_2))$, and $i\omega(c_2 + C(b/V)(\cos(\alpha_2))^2)$ as shown in Eq. (12). The process damping contribution depends on the (b/V) ratio in each case, where $V = (\pi d)/60$ (d is the workpiece diameter and Ω is expressed in rpm). Therefore, the b and Ω vectors must be known in order to modify the damping. This establishes a converging stability solution. The following steps are completed for each lobe number, N:

1. the analytical stability boundary is calculated with no process damping to identify initial b and Ω vectors
2. these vectors are used to determine the initial process damping contribution
3. the stability analysis is repeated with the new damping terms to determine updated b and Ω vectors
4. the process is repeated until the stability boundary converges.

As shown in [18–20], the solution converges rapidly (20 iterations or less is typically sufficient).

To demonstrate the algorithm, consider the model in Fig. 1 with $\alpha_1 = 30°, \alpha_2 = 60°, \beta = 70°, K_s = 2000\ \text{N/mm}^2, C = 200\ \text{N/mm}$, and $d = 75$ mm for an outer diameter turning operation. The structural dynamics are symmetric with a stiffness of 9×10^6 N/m, a natural frequency of 900 Hz, and a viscous damping ratio of 0.03 (3%). The corresponding stability limit with process damping effects is displayed in Fig. 2. To validate the predicted stability limit, Eqs. (5) and (6) were solved by Euler (numerical) integration in a time domain simulation [22]. Stable {spindle speed, chip width} combinations are identified by circles and unstable combinations are represented by squares in Fig. 2. Good agreement is observed.

2.2. Two DOF in two directions

The coupled dynamics solution is now extended to two DOF in the two orthogonal directions, u_1 and u_2. From an FRF measurement in each direction, the modal parameters can be extracted (by peak picking, for example) which represent uncoupled single DOF systems in the modal coordinates q_1 and q_2 for the u_1 direction and p_1 and p_2 for the u_2 direction [22]. This modal representation requires that proportional damping holds, but this is a reasonable approximation for the lightly damped tool dynamics typically observed in practice.

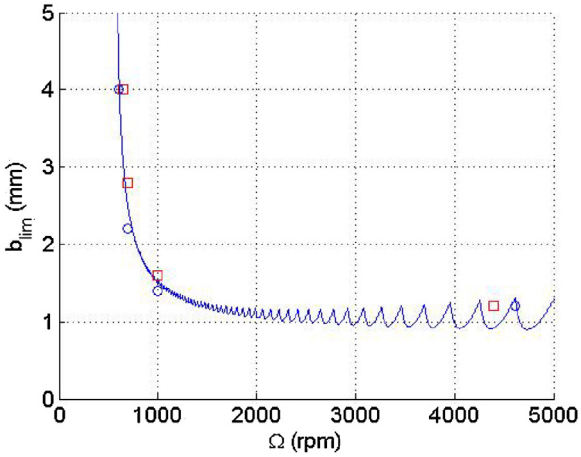

Fig. 2. Comparison of analytical stability limit and time domain simulation results for turning model with a single DOF in two orthogonal directions. Stable {spindle speed, chip width} combinations are identified by circles and unstable combinations are represented by squares.

Eq. (5), which provides the equation of motion for the u_1 direction with a single DOF, is rewritten in Eq. (17) to describe motion in the first modal DOF, q_1. The y direction velocity is again $\dot{y} = \dot{u}_1\cos(\alpha_1) + \dot{u}_2\cos(\alpha_2)$, but $\dot{u}_1$ is now the sum of the modal velocities, $\dot{u}_1 = \dot{q}_1 + \dot{q}_2$; similarly, $\dot{u}_2 = \dot{p}_1 + \dot{p}_2$. Substitution yields Eq. (18). Eqs. (19) and (20) give the results for q_2 motion (the second modal DOF) in the u_1 direction.

$$m_{q_1}\ddot{q}_1 + c_{q_1}\dot{q}_1 + k_{q_1}q_1 = F_{c_1} - C\frac{b}{V}\dot{y}\cos(\alpha_1) \tag{17}$$

$$m_{q_1}\ddot{q}_1 + c_{q_1}\dot{q}_1 + k_{q_1}q_1 = F_{c_1} - C\frac{b}{V}\cos(\alpha_1)(\cos(\alpha_1)(\dot{q}_1 + \dot{q}_2) + \cos(\alpha_2)(\dot{p}_1 + \dot{p}_2)) \tag{18}$$

$$m_{q_2}\ddot{q}_2 + c_{q_2}\dot{q}_2 + k_{q_2}q_2 = F_{c_1} - C\frac{b}{V}\dot{y}\cos(\alpha_1) \tag{19}$$

$$m_{q_2}\ddot{q}_2 + c_{q_2}\dot{q}_2 + k_{q_2}q_2 = F_{c_1} - C\frac{b}{V}\cos(\alpha_1)(\cos(\alpha_1)(\dot{q}_1 + \dot{q}_2) + \cos(\alpha_2)(\dot{p}_1 + \dot{p}_2)) \tag{20}$$

Eqs. (18) and (20) are converted to the frequency domain by again assuming harmonic motion so that $q_j(t) = Q_j e^{i\omega t}$ and $p_j(t) = P_j e^{i\omega t}$, $j = 1, 2$. Eq. (21) represents motion in Q_1 and Eq. (22) describes motion in Q_2. Even though the modal degrees of freedom are uncoupled by definition, the two equations of motion for the u_1 direction now include both Q_1 and Q_2 due to process damping. Similar to the single DOF model in the previous section, the equations also include contributions from the u_2 direction dynamics (P_1 and P_2). Interestingly, the equations of motion are coupled in both modal coordinates and the two orthogonal directions. This presents a rich dynamic system which is unlike other machining models.

$$\left(-m_{q_1}\omega^2 + i\omega\left(c_{q_1} + C\frac{b}{V}(\cos(\alpha_1))^2\right) + k_{q_1}\right)Q_1 + \left(i\omega C\frac{b}{V}(\cos(\alpha_1))^2\right)Q_2 + \left(C\frac{b}{V}\cos(\alpha_1)\cos(\alpha_2)\right)(P_1 + P_2) = F_{c_1} \tag{21}$$

$$\left(-m_{q_2}\omega^2 + i\omega\left(c_{q_2} + C\frac{b}{V}(\cos(\alpha_1))^2\right) + k_{q_2}\right)Q_2 + \left(i\omega C\frac{b}{V}(\cos(\alpha_1))^2\right)Q_1 + \left(C\frac{b}{V}\cos(\alpha_1)\cos(\alpha_2)\right)(P_1 + P_2) = F_{c_1} \tag{22}$$

Following the same approach, the frequency domain equations for the u_2 direction are presented in Eqs. (23) and (24), where Eq. (23) describes motion in P_1 and Eq. (24) describes motion in P_2.

$$\left(-m_{p_1}\omega^2 + i\omega\left(c_{p_1} + C\frac{b}{V}(\cos(\alpha_2))^2\right) + k_{p_1}\right)P_1 + \left(i\omega C\frac{b}{V}(\cos(\alpha_2))^2\right)P_2 + \left(C\frac{b}{V}\cos(\alpha_1)\cos(\alpha_2)\right)(Q_1 + Q_2) = F_{c_2} \tag{23}$$

$$\left(-m_{p_2}\omega^2 + i\omega\left(c_{p_2} + C\frac{b}{V}(\cos(\alpha_2))^2\right) + k_{p_2}\right)P_2 + \left(i\omega C\frac{b}{V}(\cos(\alpha_2))^2\right)P_1 + \left(C\frac{b}{V}\cos(\alpha_1)\cos(\alpha_2)\right)(Q_1 + Q_2) = F_{c_2} \tag{24}$$

Eqs. (21)–(24) are arranged in matrix form as shown in Eq. (25), where:

- $a_{11} = \left(-m_{q_1}\omega^2 + i\omega\left(c_{q_1} + C\frac{b}{V}(\cos(\alpha_1))^2\right) + k_{q_1}\right)$
- $a_{12} = i\omega\left(C\frac{b}{V}(\cos(\alpha_1))^2\right)$
- $a_{13} = i\omega\left(C\frac{b}{V}\cos(\alpha_1)\cos(\alpha_2)\right)$
- $a_{14} = i\omega\left(C\frac{b}{V}\cos(\alpha_1)\cos(\alpha_2)\right)$
- $a_{21} = a_{12}$
- $a_{22} = \left(-m_{q_2}\omega^2 + i\omega\left(c_{q_2} + C\frac{b}{V}(\cos(\alpha_1))^2\right) + k_{q_2}\right)$
- $a_{23} = i\omega\left(C\frac{b}{V}\cos(\alpha_1)\cos(\alpha_2)\right)$
- $a_{24} = i\omega\left(C\frac{b}{V}\cos(\alpha_1)\cos(\alpha_2)\right)$
- $a_{31} = a_{13}$
- $a_{32} = a_{23}$
- $a_{33} = \left(-m_{p_1}\omega^2 + i\omega\left(c_{p_1} + C\frac{b}{V}(\cos(\alpha_2))^2\right) + k_{p_1}\right)$
- $a_{34} = i\omega\left(C\frac{b}{V}\cos(\alpha_1)\cos(\alpha_2)\right)$
- $a_{41} = a_{14}$
- $a_{42} = a_{24}$
- $a_{43} = a_{34}$
- $a_{44} = \left(-m_{p_2}\omega^2 + i\omega\left(c_{p_2} + C\frac{b}{V}(\cos(\alpha_2))^2\right) + k_{p_2}\right)$.

$$\begin{bmatrix} a_{11} & a_{12} & a_{13} & a_{14} \\ a_{21} & a_{22} & a_{23} & a_{24} \\ a_{31} & a_{32} & a_{33} & a_{34} \\ a_{41} & a_{42} & a_{43} & a_{44} \end{bmatrix} \begin{bmatrix} Q_1 \\ Q_2 \\ P_1 \\ P_2 \end{bmatrix} = \begin{bmatrix} F_{c_1} \\ F_{c_1} \\ F_{c_2} \\ F_{c_2} \end{bmatrix} \tag{25}$$

Again using complex matrix inversion on a frequency-by-frequency basis, the direct and cross frequency response functions (FRFs) for the coupled dynamic system are obtained as shown in Eq. (26).

$$\begin{bmatrix} Q_1 \\ Q_2 \\ P_1 \\ P_2 \end{bmatrix} = \begin{bmatrix} a_{11} & a_{12} & a_{13} & a_{14} \\ a_{21} & a_{22} & a_{23} & a_{24} \\ a_{31} & a_{32} & a_{33} & a_{34} \\ a_{41} & a_{42} & a_{43} & a_{44} \end{bmatrix}^{-1} \begin{bmatrix} F_{c_1} \\ F_{c_1} \\ F_{c_2} \\ F_{c_2} \end{bmatrix}$$

$$= \begin{bmatrix} \frac{Q_{1,1}}{F_{c_1}} & \frac{Q_{1,2}}{F_{c_1}} & \frac{Q_{1,3}}{F_{c_2}} & \frac{Q_{1,4}}{F_{c_2}} \\ \frac{Q_{2,1}}{F_{c_1}} & \frac{Q_{2,2}}{F_{c_1}} & \frac{Q_{2,3}}{F_{c_2}} & \frac{Q_{2,4}}{F_{c_2}} \\ \frac{P_{1,1}}{F_{c_1}} & \frac{P_{1,2}}{F_{c_1}} & \frac{P_{1,3}}{F_{c_2}} & \frac{P_{1,4}}{F_{c_2}} \\ \frac{P_{3,1}}{F_{c_1}} & \frac{Q_{2,3}}{F_{c_1}} & \frac{P_{2,3}}{F_{c_2}} & \frac{P_{2,4}}{F_{c_2}} \end{bmatrix} \begin{bmatrix} F_{c_1} \\ F_{c_1} \\ F_{c_2} \\ F_{c_2} \end{bmatrix} \tag{26}$$

The direct FRFs in the u_1 and u_2 directions are defined by Eqs. (27) and (28), respectively; the cross FRFs are provided in Eqs. (29) and (30). The oriented FRF is again calculated using Eq. (16) and the directional orientation factors are the same.

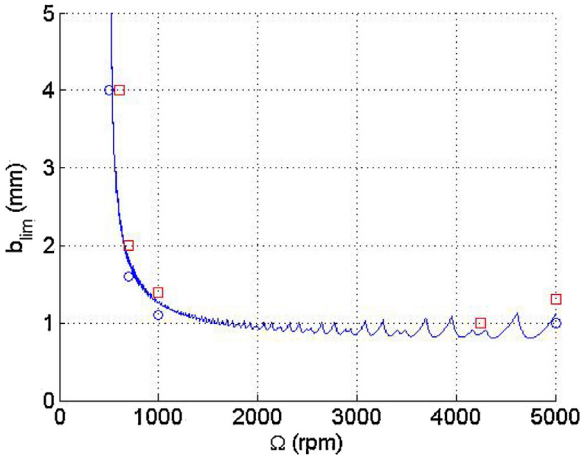

Fig. 3. Comparison of analytical stability limit and time domain simulation results for turning model with two DOF in two orthogonal directions.

$$\frac{U_1}{F_{c_1}} = \frac{Q_{1,1}}{F_{c_1}} + \frac{Q_{1,2}}{F_{c_1}} + \frac{Q_{2,1}}{F_{c_1}} + \frac{Q_{2,2}}{F_{c_1}} \tag{27}$$

$$\frac{U_2}{F_{c_2}} = \frac{P_{1,3}}{F_{c_2}} + \frac{P_{1,4}}{F_{c_2}} + \frac{P_{2,3}}{F_{c_2}} + \frac{P_{2,4}}{F_{c_2}} \tag{28}$$

$$\frac{U_2}{F_{c_1}} = \frac{P_{1,1}}{F_{c_1}} + \frac{P_{1,2}}{F_{c_1}} + \frac{P_{2,1}}{F_{c_1}} + \frac{P_{2,2}}{F_{c_1}} \tag{29}$$

$$\frac{U_1}{F_{c_2}} = \frac{Q_{1,3}}{F_{c_2}} + \frac{Q_{1,4}}{F_{c_2}} + \frac{Q_{2,3}}{F_{c_2}} + \frac{Q_{2,4}}{F_{c_2}} \tag{30}$$

The model may be extended to additional DOFs in each direction. For three DOFs in each direction, for example, Eq. (25) becomes a 6×6 symmetric matrix. The direct and cross FRFs are then a sum of six, rather than four, terms from the inverted matrix.

To demonstrate the multiple DOF algorithm, consider the model in Fig. 1 with $\alpha_1 = 30°$, $\alpha_2 = 60°$, $\beta = 70°$, $K_s = 2000\,\text{N/mm}^2$, $C = 200\,\text{N/mm}$, and $d = 75\,\text{mm}$ for an outer diameter turning operation. The structural dynamics are symmetric with a modal stiffness of $7 \times 10^6\,\text{N/m}$, a natural frequency of 600 Hz, and a viscous modal damping ratio of 0.03 (3%) for the first mode and a modal stiffness of $9 \times 10^6\,\text{N/m}$, a natural frequency of 900 Hz, and a viscous modal damping ratio of 0.03 (3%) for the second mode. The corresponding stability limit with process damping effects is displayed in Fig. 3. To validate the predicted stability limit, the modal equations of motion were solved by Euler (numerical) integration in a time domain simulation [22]. Stable {spindle speed, chip width} combinations are identified by circles and unstable combinations are represented by squares in Fig. 3. Good agreement is observed.

3. Experimental set-up

Low-speed cutting tests were performed in order to validate the multiple degree of freedom process damping model and calculate a process damping coefficient. The experiments were carried out on a Haas TL-1 CNC lathe. A custom notch hinge flexible cutting tool was designed to provide a multiple degree of freedom (DOF) system in the feed direction of the cutting operation; see Fig. 4.

A tube turning geometry was selected for the cutting tests. In this arrangement, the feed direction is parallel to the tube axis. Because the flexure compliance was much higher than the workpiece in the feed direction, the stability analysis was completed using the flexure's dynamic properties only. The frequency response function and modal parameters for the flexure in the feed and tangential

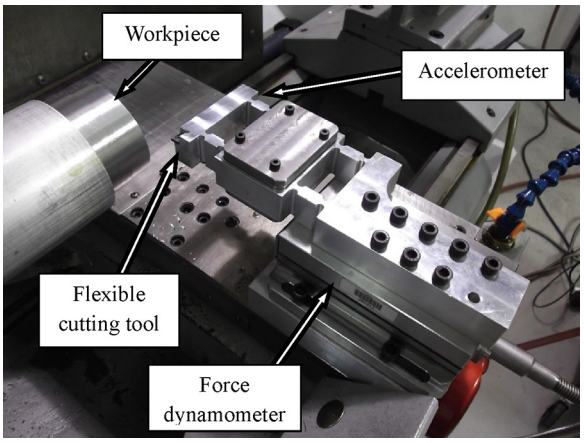

Fig. 4. Experimental setup for turning stability tests. A cutting force dynamometer and accelerometer (not shown) were used to monitor the cutting process.

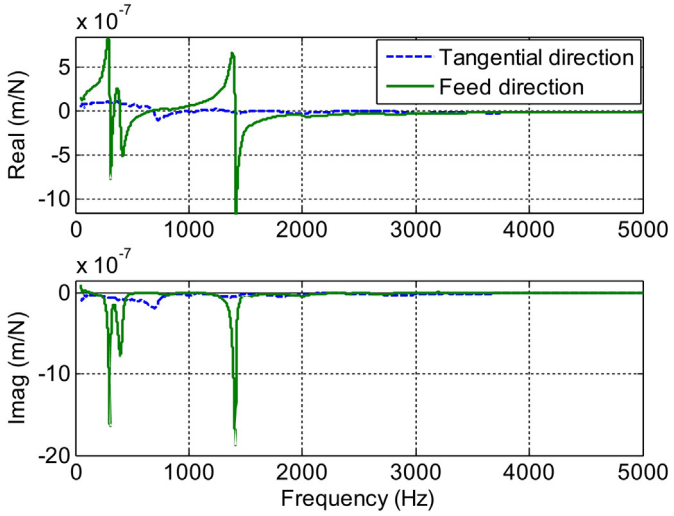

Fig. 5. Frequency response function of flexible cutting tool in tangential and feed directions.

directions are provided in Fig. 5 and Table 1. These were determined using impact testing, where an instrumented hammer is used to excite the structure and the response is measured using a linear transducer (a low mass accelerometer in this case).

The workpiece material for all cutting tests was 6061-T6 aluminum. The wall thickness of the tube was varied, while a constant mean workpiece diameter of 87 mm was maintained for all experiments. The cutting insert (Kennametal SPEB322) was TiN coated with an 11 deg relief angle, 0 deg rake angle, and no chip breaker. The commanded chip width, b, varied between 1.0 mm and 3.0 mm and the cutting speed range was 82–273 m/min (300–1000 rpm). The feed rate was held constant at 0.13 mm/rev.

Table 1
Modal parameters for flexible cutting tool setup.

Direction	Viscous damping ratio (%)	Modal stiffness ($\times 10^7$ N/m)	Natural frequency (Hz)
Tangential	7.21	3.71	703
	6.23	0.80	303
Feed	9.01	0.96	405
	1.68	1.88	1433

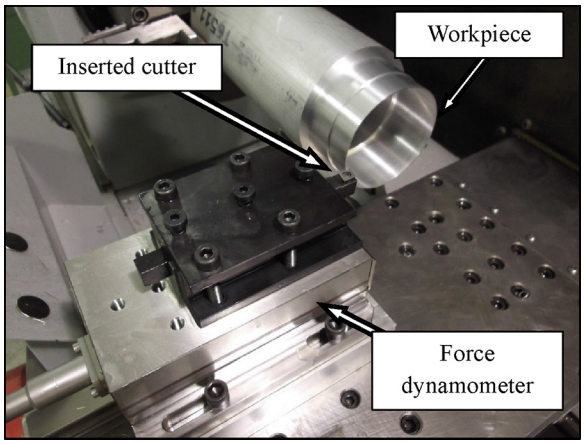

Fig. 6. Experimental setup used to identify the force model for the selected tool/workpiece combination.

4. Experimental results

Before stability testing was completed, the force model for the workpiece/cutter combination was identified. This was achieved under stable cutting conditions using an off-the-shelf lathe insert holder that held the same insert as the manufactured flexible tool. The inserted holder was mounted to the cutting force dynamometer (Fig. 6). The force model was calculated at both 500 and 1000 rpm for $b = 1$ mm and feed rate of 0.13 mm/rev. The mean values were $K_s = 1343 \pm 32$ N/mm^2 (which scales the chip area to obtain the resultant cutting force) and $\beta = 55^\circ$ (the force angle).

The stability was identified using an accelerometer (PCB Piezotronics model 352B10) and cutting force dynamometer (Kistler model 9257B). The force and vibration levels, as well as the frequency content of the two signals, were used to establish stable/unstable performance. Also, qualitatively, the machined surface finish after each test cut was inspected using a digital microscope.

4.1. Process damping coefficient

A grid of low-speed test points was selected to investigate the process damping behavior for the multi-degree of freedom system; see Fig. 7. Points A and B in Fig. 7 were selected to illustrate the characteristics of stable and unstable cutting conditions. Fig. 8 presents the force and acceleration signals for point A ($V = 82.1$ m/min, $\Omega = 300$ rpm, $b = 3$ mm). It was observed that the force for this

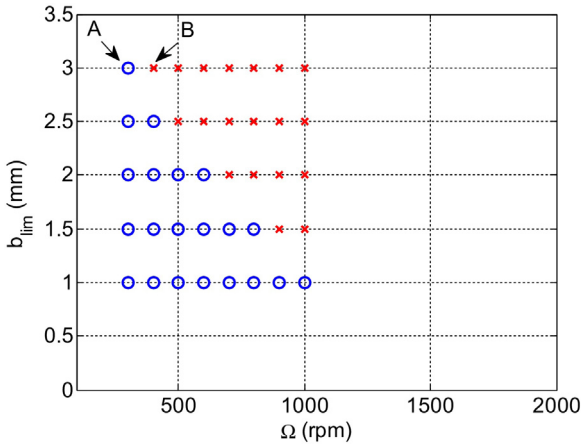

Fig. 7. Grid of stable (o) and unstable (×) chip width/spindle speed combinations.

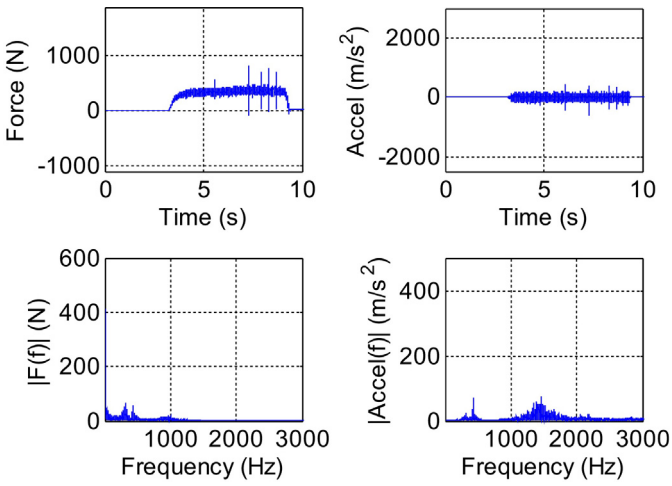

Fig. 8. (Top row) Cutting force and accelerometer time domain signals in the feed direction for the stable point A {300 rpm, 3.0 mm} with (bottom row) corresponding frequency content.

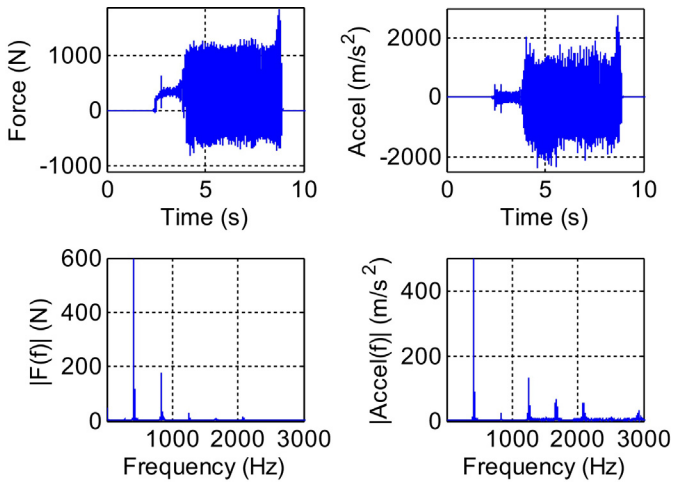

Fig. 9. (Top row) Cutting force and accelerometer time domain signals in the feed direction for the unstable point B {400 rpm, 3.0 mm} with (bottom row) corresponding frequency content. The chatter frequency is approximately 310 Hz.

stable cut remained steady at a mean of approximately 364 N with no apparent growth or instability in the time domain. The frequency content of the force and accelerometer signals at point A reveal small, but not distinct, peaks near the flexure's natural frequencies.

Point B in Fig. 7 represents an unstable cut ($V = 109.5$ m/min, $\Omega = 400$ rpm, $b = 3.0$ mm). Fig. 9 displays the force and vibration signals. A substantial increase in force and acceleration are observed after approximately one second of cutting. The fundamental chatter frequency, $f_c = 310$ Hz, is near the first vibration mode of the flexure-based tool.

4.2. Machined surface and chip morphology

Fig. 10 presents the surface finish and chip morphology for a typical stable test. The digital microscope image in Fig. 10b displays an end view of the cut tube; a smooth surface with no apparent chatter vibrations is observed. The chips are smooth and continuous due to the absence of a chip-breaker.

Fig. 11 shows the surface and chip morphology for an unstable cut. The digital microscope image in Fig. 11b displays the large undulations due to chatter. The chips contain similar undulations and are irregular and discontinuous due to the large vibration levels; see Fig. 11c.

A process damping coefficient, C, was estimated based on a single variable residual sum of squares (RSS) minimization that best represented the stability boundary [20]. The stability boundary and grid of stable/unstable test points are presented in Fig. 12. A process damping coefficient value of $C = 1.3 \times 10^5$ N/m was found to best represent the stability boundary. It is interesting to note the intersection of the stability boundary caused by the two vibratory

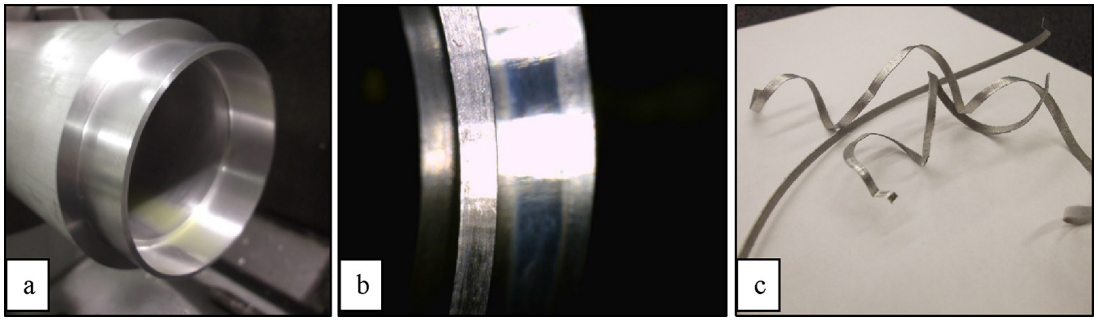

Fig. 10. Machined surface and chip morphology for a stable cut.

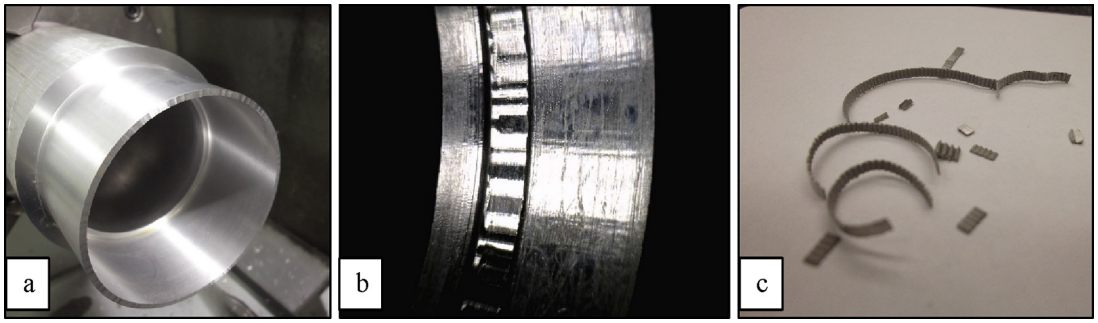

Fig. 11. Machined surface and chip morphology for an unstable cut.

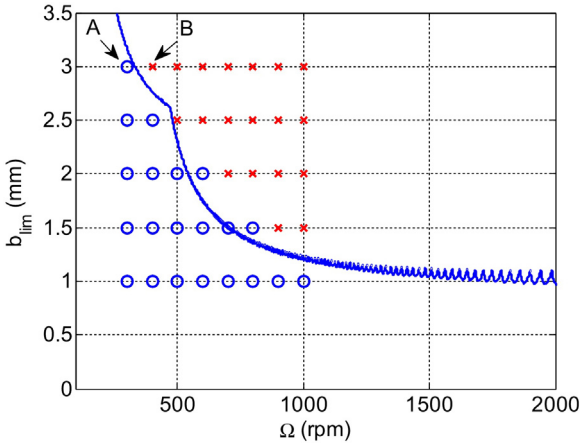

Fig. 12. Stability boundary for the multi-degree of freedom system with the grid of stable (o) and unstable (×) cutting tests ($C = 1.3 \times 10^5$ N/m).

Table 2
Modal parameters for subsequent turning tests.

Direction	Viscous damping ratio (%)	Modal stiffness ($\times 10^7$ N/m)	Natural frequency (Hz)
Tangential	7.21	3.71	703
	3.56	0.85	304
Feed	5.46	1.17	394
	0.99	2.69	1410

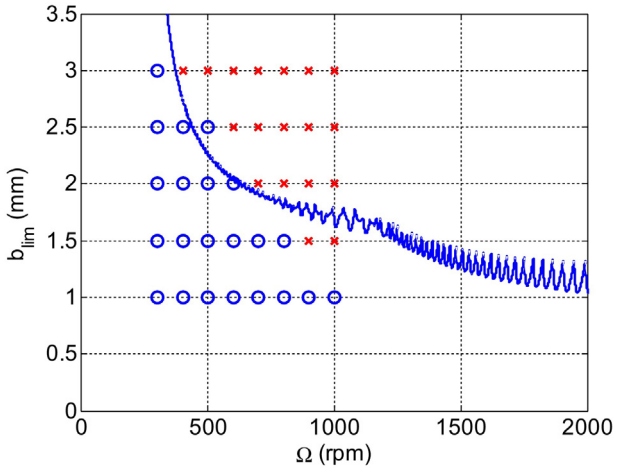

Fig. 13. Grid of stable (o) and unstable (×) test points with the final stability boundary corresponding to $C = 2.6 \times 10^5$ N/m.

modes that occurs at approximately 500 rpm in this experiment. In fact, it is the lower stability boundary (corresponding to the more flexible vibration mode) that truncates the upper stability boundary (corresponding to the stiffer vibration mode) and largely influences the process damping coefficient value.

In subsequent testing of the multiple DOF turning setup, the dynamics of the system were changed slightly when the flexure was removed from the dynamometer and replaced; see Table 2. In particular, the damping ratios in the feed direction decreased. A similar grid of $\{b, \Omega\}$ combinations were tested for the new setup and the stability was analyzed. A process damping coefficient of $C = 2.6 \times 10^5$ N/m was calculated to best fit the grid of test points. However, it was observed that the grid of stable and unstable points changed relatively little between the two tests; see Fig. 13. Due to the slight changes in dynamics, the intersection of the stability boundaries also changes. The intersection of the two stability boundaries, which occurred at approximately 500 rpm and 2.5 mm previously, now occurs near 1200 rpm and 1.5 mm. The stability boundary is truncated in such a way that it is now the upper boundary (corresponding to the stiffer vibration mode) which limits the allowable chip width at most speeds and, therefore, dictates the best fit process damping coefficient.

It is concluded that there is a decision to make when analyzing multiple DOF systems. Either the user can fit the stability boundary while taking into consideration all modes of vibration or the user can consider only the most flexible mode of vibration when calculating the process damping coefficient. The former method may lead to higher, perhaps artificial, process damping coefficient values. The latter method, choosing the more flexible vibration mode, yields process damping values which have been shown to agree well with single and multiple DOF milling systems using a similar experimental approach [23].

5. Conclusions

An analytical stability model was presented which accounts for multiple degree of freedom vibratory systems in turning applications. The model includes a process damping force in the surface normal direction which depends on the depth of cut, the cutting speed, the tool velocity, and an empirical process damping coefficient, C.

The analytical model was validated using time domain simulation and experiments. Stability testing was completed using a custom parallelogram notch hinge flexure-based cutting tool to machine a tubular workpiece. The cutting tool was designed to have multiple vibratory modes in the feed direction. Cutting force and vibration signals were used to distinguish between stable and unstable cutting conditions for a defined grid of low spindle speed, chip width pairs. Using the most flexible vibration mode, a process damping coefficient of $C = 1.3 \times 10^5$ N/m was calculated to best fit the grid of test points using a residual sum of squares minimization for 6061-T6 aluminum. It was concluded that in a multiple degree of freedom scenario the most flexible mode of vibration should be used when identifying the process damping coefficient.

Process damping is particularly important for cutting hard-to-machine materials, as well as machining processes that are limited to low cutting velocities such as turning. By exploiting process damping, higher stable depths of cut can be achieved. Knowledge of process damping coefficients for particular materials enables pre-process selection of machining parameters that provide high productivity.

Acknowledgements

The authors gratefully acknowledge partial financial support from the University of North Carolina at Charlotte Center for Precision Metrology Affiliates Program.

References

[1] Wallace PW, Andrew C. Machining forces: some effects of tool vibration. J Mech Eng Sci 1965;7:152–62.
[2] Sisson TR, Kegg RL. An explanation of low-speed chatter effects. J Eng Ind 1969;91:951–8.
[3] Peters J, Vanherck P, Van Brussel H. The measurement of the dynamic cutting coefficient. Ann CIRP 1971;21/2:129–36.
[4] Tlusty J. Analysis of the state of research in cutting dynamics. Ann CIRP 1978;27/2:583–9.
[5] Wu DW. A new approach of formulating the transfer function for dynamic cutting processes. J Eng Ind 1989;111:37–47.
[6] Elbestawi MA, Ismail F, Du R, Ullagaddi BC. Modelling machining dynamics damping in the tool-workpiece interface. J Eng Ind 1994;116:435–9.
[7] Lee BY, Trang YS, Ma SC. Modeling of the process damping force in chatter vibration. Int J Mach Tools Manuf 1995;35:951–62.

[8] Abraria F, Elbestawi MA, Spencea AD. On the dynamics of ball end milling: modeling of cutting forces and stability analysis. Int J Mach Tools Manuf 1998;38:215–37.
[9] Ahmadi K, Ismail F. Machining chatter in flank milling. Int J Mach Tools Manuf 2010;50:75–85.
[10] Huang CY, Wang JJ. Mechanistic modeling of process damping in peripheral milling. J Manuf Sci Eng 2007;129:12–20.
[11] Chiou YS, Chung ES, Liang SY. Analysis of tool wear effect on chatter stability in turning. Int J Mech Sci 1995;37:391–404.
[12] Chiou RY, Liang SY. Chatter stability of a slender cutting tool in turning with tool wear effect. Int J Mach Tools Manuf 1998;38:315–27.
[13] Chandiramani NK, Pothala T. Dynamics of 2-dof regenerative chatter during turning. J Sound Vib 2006;290:448–64.
[14] Jemielniak K, Widota A. Numerical simulation of non-linear chatter vibration in turning. Int J Mach Tools Manuf 1989;29:239–47.
[15] Ahmadi K, Ismail F. Experimental investigation of process damping nonlinearity in machining chatter. Int J Mach Tools Manuf 2010;50:1006–14.
[16] Budak E, Tunc LT. A new method for identification and modeling of process damping in machining. J Manuf Sci Eng 2009;131, 051019/1-10.
[17] Altintas Y, Eynian M, Onozuka H. Identification of dynamic cutting force coefficients and chatter stability with process damping. Ann CIRP 2008;57/1:371–4.
[18] Tyler C, Schmitz T. Process damping analytical stability analysis and validation. Trans NAMRI/SME 2012;40.
[19] Tyler C, Karandikar J, Schmitz T. Process damping coefficient identification using Bayesian inference. Trans NAMRI/SME 2013;41.
[20] Tyler C, Schmitz T. Analytical process damping stability prediction. J Manuf Process 2013;15:69–76.
[21] Tlusty J, Polacek M. The stability of machine tools against self-excited vibrations in machining. In: Proceedings of the ASME International Research in Production Engineering Conference. 1963. p. 465–74.
[22] Schmitz T, Smith S. Machining dynamics: frequency response to improved productivity. New York, NY: Springer; 2009.
[23] Tyler C, Troutman J, Schmitz T. A coupled dynamics, multiple degree of freedom process damping model, Part 2: Milling. Precis Eng 2016;46:73–80.